Monthly Notices
of the
ROYAL ASTRONOMICAL SOCIETY

Mon. Not. R. Astron. Soc. **400,** 820–834 (2009) doi:10.1111/j.1365-2966.2009.15502.x

On the magnetization of jet-launching discs

P. Tzeferacos,[1⋆] A. Ferrari,[1,2] A. Mignone,[1,3] C. Zanni,[3,4] G. Bodo[3] and S. Massaglia[1]

[1]*Dipartimento di Fisica Generale, Università degli Studi di Torino, Via Giuria 1, 10125 Torino, Italy*
[2]*Department of Astronomy and Astrophysics, University of Chicago, USA*
[3]*INAF – Osservatorio Astronomico di Torino, Viale Osservatorio 20, 10025 Pino Torinese, Italy*
[4]*Laboratoire d'Astrophysique de Grenoble, 414 rue de la Piscine, BP 53, 38041 Grenoble, France*

Accepted 2009 August 3. Received 2009 August 3; in original form 2009 April 22

ABSTRACT

Magnetohydrodynamic models of collimated outflows produced by accretion discs around compact objects can be used for interpreting the phenomenology of active astrophysical objects as young stellar objects, microquasars, X-ray binaries, gamma-ray bursts, extended radio galaxies and active galactic nuclei. In the present work, we discuss how the strength of magnetic fields determines the characteristics of solutions in models where the collimated outflow and the accretion disc are treated consistently. We perform an extensive analysis of the magnetic field's strength by non-relativistic axisymmetric numerical simulations using the PLUTO code. We discuss in detail the characteristics of the numerical solutions with specific reference to the efficiency of transforming accretion inflows into collimated superfast magnetosonic outflows. The relevance of the resistivity parameter used in numerical simulations is analysed. The main results are that magnetic fields around and below equipartition with plasma pressure allow for steady superfast magnetosonic collimated jet solutions; for even lower magnetization, the solutions found are unsteady, with small velocities and matter-dominated magnetic field lines that behave kinematically; magnetic fields above equipartition lead to unsteady sub-Alfvénic winds. These results allow to conclude that stationary super-Alfvénic and superfast magnetosonic outflow solutions are found only for equipartition and weaker magnetic fields, for the range studied in this article.

Key words: accretion, accretion discs – MHD – methods: numerical – ISM: jets and outflows.

1 INTRODUCTION

Young stellar objects (YSO), microquasars, X-ray binaries, gamma-ray bursts (GRB), extended radio galaxies and active galactic nuclei (AGN) are characterized by the presence of supersonic outflows and collimated jets. In all these scenarios, outflows are associated with inflows on to a central compact object with a strong gravitational pull. The outflow velocities are typically of the order of the escape velocity from the central attractors; therefore, in the case of the most active and relativistic jets the central attractors are most likely black holes. The most acknowledged models for interpreting the origin of astrophysical supersonic and relativistic jets are based on the interaction of large-scale magnetic fields with an accreting quasi-Keplerian disc. In fact, although supersonic velocities can be reached by purely hydrodynamic mechanisms or by radiation pressure, outflows with large Lorentz factors can only be explained by the intervention of electromagnetic effects.

⋆E-mail: petros.tzeferacos@ph.unito.it

Lovelace (1976) and Blandford (1976) showed that a force-free poloidal field anchored in a Keplerian disc can extract energy and angular momentum creating a Poynting flux jet that accelerate a plasma current along the disc funnel up to relativistic speeds. This idea was developed in the magnetohydrodynamic regime including the matter's inertia by Blandford & Payne (1982), who showed how Poynting jets can transfer their energy and momentum to matter outflows via a magnetocentrifugal mechanism capable of reaching superfast magnetosonic speeds. Later on, Vlahakis & Tsinganos (1998) reconstructed the classes of meridionally and radially self-similar solutions of MHD outflows in a systematic way. In these works, the disc was considered as a fixed boundary and no self-consistent treatment of the whole inflow/outflow dynamics was attempted.

Poynting flux solutions, usually applied to extended radio sources and AGN jets whose densities appear much lighter than the ambient medium, were also found for rapidly rotating magnetized stars in the propeller regime, used to describe young T Tauri stars (Romanova et al. 2005; Ustyugova et al. 2006; Romanova et al. 2009). These outflows were also accompanied by matter-dominated conical winds from the inner disc, both for rapidly and slowly

rotating stars (Romanova et al. 2009). On the other hand, the MHD case with relatively dense jets carrying inertia is of more general application for all types of jets. In particular, recent works aim to derive for which configurations of accretion discs the MHD launching of the jet may occur. For instance, Ferreira & Pelletier (1995), Ferreira (1997) and Casse & Ferreira (2000a) have studied analytic 'cold' steady-state outflow solutions linked to accreting slim discs including viscous and resistive effects in the discs and allowing for anisotropic magnetic diffusivity between poloidal and toroidal fields; they conclude that superfast magnetosonic outflows can be obtained with plasma β values around unity, for a limited range of Prandtl numbers and larger toroidal diffusivity. Similarly, Ogilvie & Livio (2001) investigated the effect of the vertical structure of a cold disc in equilibrium with an isothermal corona considering also different topologies of the poloidal field; they showed that substantial outflow rates are generated only for magnetic fields around equipartition and with the poloidal component exiting at angles around 30°–50° from the disc.

Numerical simulations allow instead to investigate time-dependent solutions, although they are often still limited to the study of the origin of the outflow treating the disc as a boundary condition (Ouyed & Pudritz 1997; Krasnopolsky, Li & Blandford 1999; Ustyugova et al. 1999), or referred to the entire disc–jet system but for very short time-scales (Uchida & Shibata 1985; Kato, Kudoh & Shibata 2002). Casse & Keppens (2002) have followed the evolution of an accretion–ejection system for longer time-scales but with the energy equation replaced by a simple polytropic equation of state; more recently, they updated their work including some non-adiabatic effects (Casse & Keppens 2004).

At present, the stability of configurations of jet-driving magnetized discs is still under discussion. An interesting approach on this issue has been proposed by Königl (2004) working out a stability criterion that shows the existence of a class of stable solutions of the self-similar Blandford & Payne model.

In this paper, we address the problem of stationarity of the inflow/outflow dynamics on the basis of compressible MHD numerical simulations, analysing the effects of the most relevant physical parameters with respect to the possibility of reaching steady-state solutions over long time-scales of integration. In a previous paper, Zanni et al. (2007) have discussed the importance of resistive effects on the solutions. Here, we will mostly concentrate on the strength and configuration of the initial magnetic field associated with the accretion disc. Simulations have been performed for a 2.5-dimensional configuration making use of the numerical code PLUTO[1] (Mignone et al. 2007). We will concentrate our discussion on the non-relativistic dynamics of a jet-driving disc. The interaction with the central object and the outflows which could possibly emerge from this part of the system will be neglected.

The plan of the paper is the following. In Section 2, we discuss the equations governing our model and how they are implemented in the numerical scheme. In Section 3, we study solutions for different values of the magnetization parameter $\mu = B^2/2P$ and show how steady or intermittent collimated jets are produced for magnetic fields below equipartition, while stronger fields give rise to sub-Alfvénic winds from the accretion disc. In Section 4, we come back to the problem of magnetic diffusivity and its anisotropy, that, however, appears to be less crucial than suggested in previous works. Finally, we discuss the relevance of our result for astrophysical applications and future directions of analysis.

[1] http://plutocode.to.astro.it

2 SETUP

2.1 MHD equations

In order to model the accretion ejection system, we solve numerically the equations of resistive MHD. We present here the form adopted in our numerical calculations.

The first equation represents conservation of mass:

$$\frac{\partial \rho}{\partial t} + \nabla \cdot (\rho \boldsymbol{u}) = 0, \tag{1}$$

where we denote with ρ the mass density and $\boldsymbol{u}$ the speed of the flow.

The momentum conservation reads

$$\frac{\partial (\rho \boldsymbol{u})}{\partial t} + \nabla \cdot \left[\rho \boldsymbol{u}\boldsymbol{u} + \left(P + \frac{\boldsymbol{B}\cdot\boldsymbol{B}}{2} \right) \boldsymbol{I} - \boldsymbol{B}\boldsymbol{B} \right] + \rho \nabla \Phi_{\rm g} = 0. \tag{2}$$

The forces taken into account are the thermal pressure gradient, the Lorentz force and the gravitational force. The gravitational potential created by the central object of mass M is given in cylindrical coordinates by $\Phi_{\rm g} = -GM/\sqrt{r^2+z^2}$.

The evolution of the magnetic field is governed by the induction equation:

$$\frac{\partial \boldsymbol{B}}{\partial t} + \nabla \times \boldsymbol{E} = 0, \tag{3}$$

where the electric field is given by Ohm's law, $\boldsymbol{E} = -\boldsymbol{u} \times \boldsymbol{B} + \bar{\bar{\eta}} : \boldsymbol{J}$ and the current $J = \nabla \times \boldsymbol{B}$ is given by Ampere's law. We assume that the magnetic resistivity is a diagonal tensor η_{ij} whose non-zero components are $\eta_{\phi\phi} = \eta_{\rm m}$ and $\eta_{rr} = \eta_{zz} = \eta'_{\rm m}$.

The equation that accounts for the energy budget of the system is

$$\frac{\partial e}{\partial t} + \nabla \cdot \left[\left(e + P + \frac{\boldsymbol{B}\cdot\boldsymbol{B}}{2} \right) \boldsymbol{u} - (\boldsymbol{u}\cdot\boldsymbol{B})\boldsymbol{B} + (\bar{\bar{\eta}} : \boldsymbol{J}) \times \boldsymbol{B} \right] = -\Lambda_{\rm cool}, \tag{4}$$

where e denotes the total energy density which is given by

$$e = \frac{P}{\gamma - 1} + \frac{\rho \boldsymbol{u}\cdot\boldsymbol{u}}{2} + \frac{\boldsymbol{B}\cdot\boldsymbol{B}}{2} + \rho \Phi_{\rm g}. \tag{5}$$

We close the system with an ideal gas equation of state, taking the specific heat ratio γ equal to 5/3 (the disc is considered adiabatic). In the last equation, the four terms are the internal, kinetic, magnetic and gravitational energy, respectively. The term $\Lambda_{\rm cool}$ is a cooling function which in our study will be assumed proportional to the Ohmic heating term $\Lambda_{\rm ohm} = f(\bar{\bar{\eta}} : \boldsymbol{J}) \cdot \boldsymbol{J}$. We take the factor f always equal to 1, which effectively means that all Ohmic heating is radiated away. We have chosen not to include the effects of turbulent viscosity. If the Prandtl number is of the order of unity and the magnetization is in the range considered in this paper, the viscous torque can be neglected, as both analytical (Casse & Ferreira 2000a) and numerical (Meliani, Casse & Sauty 2006) studies have previously shown.

2.2 Model description

The initial configuration adopted in our simulations considers a thin-disc rotating at slightly sub-Keplerian speed with a given embedded magnetic field with purely poloidal field lines exiting at some angle from the disc surface. On top, a rarefied corona lies in equilibrium with the disc's surface. The profiles of all primitive variables are derived starting from an equatorial radial self-similarity assumption.

This is done by imposing a force equilibrium in both radial and vertical directions, as dictated by the following equations:

$$\frac{\partial P}{\partial r} = -\rho \frac{\partial \Phi_{\rm g}}{\partial r} + J_\phi B_z + \frac{\rho u_\phi^2}{r}, \tag{6}$$

$$\frac{\partial P}{\partial z} = -\rho \frac{\partial \Phi_{\rm g}}{\partial z} - J_\phi B_r. \tag{7}$$

Physical quantities in the radial self-similar case follow power laws that for $z = 0$ are of the form

$$a = a_0 \left(\frac{r}{r_0}\right)^{\beta_a}, \tag{8}$$

where β_a defines the scaling. Imposing an initial polytropic relationship between density and pressure $P = P_0(\rho/\rho_0)^\gamma$ (ρ_0 is the fiducial density at the inner radius of the disc), the power-law coefficients β_a are $-1/2$ for the three components of the flow speed (the scaling of Keplerian velocity), $-5/4$ for the components of the magnetic field, $-5/2$ for the gas pressure and $-3/2$ for the density. With this choice, the radial dependence for the mid-plane temperature will in turn follow a scaling of r^{-1}.

The reconstruction of the profiles throughout the computational domain is done by specifying the initial magnetic field through its flux function which ensures that $\nabla \cdot \boldsymbol{B} = 0$:

$$\Psi = \frac{4}{3} B_{z0} r_0^2 \left(\frac{r}{r_0}\right)^{3/4} \frac{m^{5/4}}{(m^2 + z^2/r^2)^{5/8}}. \tag{9}$$

The components of the magnetic field are then written as

$$B_z = \frac{1}{r}\frac{\partial \Psi}{\partial r}, \qquad B_r = -\frac{1}{r}\frac{\partial \Psi}{\partial z}. \tag{10}$$

The parameter m determines the initial bending of the magnetic field lines whereas the coefficients B_{z0} and r_0 are derived through normalization as shown in the Appendix. The values of B_{z0} and P_{z0} define the plasma parameter β evaluated at the disc mid-plane. We will use its inverse, the magnetization parameter $\mu = B^2/2P$ to define the strength of the magnetic field. Note that this value is half of that used in the analytical formalism of Ferreira & Pelletier (1995), Ferreira (1997) and Casse & Ferreira (2000a).

There are different choices in the initialization of the magnetic's field inclination. The most obvious would be a current-free vertical field which would evolve on accretion time-scales to a bent configuration favourable for a centrifugal launching (Casse & Keppens 2002; Zanni et al. 2004). None the less, such a choice would not be favourable for a magnetization study since it would require a radial stratification of μ. Imposing a constant magnetization profile at the equator ($B_z \propto r^{-5/4}$), we must add a proper field bending (controlled by m) and curvature to obtain a force-free field in the corona. Furthermore, since the corona itself is rarefied (characteristic speeds are high) the initial poloidal configuration would rapidly evolve into a current-free configuration, equal to force free for purely poloidal fields. On the other hand, the inclination of the field lines has to be supported by an appropriate advection inside the disc. More specifically, a large magnetic Reynolds number $\mathcal{R}_{\rm m} = r u_r/\eta_{\rm m}$ is needed. Note that this bending, for our choice of m discussed later on, also satisfies the Blandford & Payne criterion (Blandford & Payne 1982) at the disc's surface. This turns out to be an important advantage since it allows us to study the magnetocentrifugal launching from the early stages of our simulations.

Given the magnetic field, we proceed by calculating the current explicitly, simply using the equation $\boldsymbol{J} = \nabla \times \boldsymbol{B}$. Since the initial magnetic field is purely poloidal, the only component of the current is toroidal. Using the vertical equilibrium equation (7) and the equation of state, we extract the disc density and pressure profile, utilizing the solution provided by the self-similar model in the equator. The thermal height scale will be proportional to the radial distance r according to the equation $H = \epsilon r$ where $\epsilon = c_{\rm s}/V_{\rm K}$ is the ratio of the isothermal sound speed $c_{\rm s} = \sqrt{P/\rho}$ and the Keplerian velocity $V_{\rm K} = \sqrt{GM/r}$, both evaluated at the disc mid-plane. On the other hand, the radial equilibrium, equation (6), yields the toroidal component of the velocity vector, whereas through the induction equation (3) we calculate the poloidal part given the relation $u_z = u_r z/r$. This last calculation requires the definition of the resistivity tensor. The disc resistivity is expressed following the paradigm of Shakura & Sunyaev (1973) for diffusion (as employed also by Casse & Keppens 2002, 2004; Zanni et al. 2007), describing the azimuthal component of the $\bar{\bar{\boldsymbol{\eta}}}$ tensor as

$$\eta_{\rm m} = \alpha V_{\rm A} H \exp\left(-2\frac{z^2}{H^2}\right), \tag{11}$$

where α is the magnetic diffusivity parameter, while $V_{\rm A} = B_z/\sqrt{\rho}$ is the Alfvén speed and $H = c_{\rm s}/\Omega_{\rm K}$ is the disc's thermal scaleheight, both evaluated at the equator. The vertical and radial components are assumed equal to $\eta'_{\rm m}$ and are defined through the anisotropy parameter $\chi_{\rm m} = \eta'_{\rm m}/\eta_{\rm m}$. This is the inverse of the parameter used in Ferreira & Pelletier (1995). The constant $\chi_{\rm m}$ will also be included in our parameter study.

Above the disc we impose a radially stratified atmosphere initially in hydrostatic equilibrium; the density and pressure profiles for the atmosphere are consistently

$$\rho_a = \rho_{a0}\left(\frac{1}{\sqrt{r^2+z^2}}\right)^{1/\gamma - 1}, \quad P_a = P_{a0}\left(\frac{\rho_a}{\rho_{a0}}\right)^\gamma. \tag{12}$$

The constant ρ_{a0} is the density of the atmosphere at the radius $R = r_0$, which is assumed δ times lighter than the disc's fiducial density ρ_0. The correlation between the two will be $\rho_{a0} = \delta\rho_0$. The temperature of the corona will then scale with the spherical radius $R = \sqrt{r^2+z^2}$ as $1/R$. The equilibrium region between the atmospheric and disc pressure defines the disc's initial surface.

2.3 Numerical setup

The parameter study of our model is carried out using the finite volume, shock capturing numerical code PLUTO (Mignone et al. 2007). Our domain is a rectangular region spanning radially from 0 to $40r_0$ and vertically from 0 to $120r_0$. A uniform resolution of [512 $\times$ 1536] is used throughout the domain, in contrast to the previous Adaptive Mesh Refinement (AMR) approach, adopted by Zanni et al. (2007). The system is allowed to evolve for 400 time units t_0. The latter is defined through spatial and velocity normalization, i.e. $t_0 = r_0/V_0$, as the time needed for the plasma to cover a distance equal to the inner disc radius, moving with the Keplerian speed at that radius (see also the Appendix). This, given the differential rotation profile described previously, translates to $\sim$63 rotations of the innermost part of the disc ($r = r_0$), whereas the outer part ($r = 40r_0$) has only performed $\sim$1/4 revolutions.

The upwind constrained transport (UCT) scheme (Londrillo & Del Zanna 2004) is chosen to handle the induction equation for the magnetic field and maintain solenoidality ($\nabla \cdot \boldsymbol{B} = 0$) at machine accuracy. For the computation of the upwind fluxes, we utilize a combination of the Harten-Lax-van Leer (HLL) and HLL-contact Riemann solvers. We apply a Van Leer limiter for the primitive variables, while a second-order Runge–Kutta method is used for temporal integration.

Axisymmetry is assumed on the rotation axis $r = 0$ whereas equatorial symmetry is supposed at the disc's mid-plane $z = 0$. At the right boundary of the domain, we specify outflow, zero-gradient conditions for the density, thermal pressure and poloidal component of the velocity vector. Instead, we retain the first derivative of u_ϕ, B_z, B_ϕ and B_r is set to satisfy solenoidality. The non-zero-gradient condition for the magnetic field is required to avoid that boundary effects produce an artificial collimation, a subject extensively discussed in Ustyugova et al. (1999). For zero-gradient condition, the magnetic pressure $\nabla(B^2/2)$ would vanish whereas the collimating hoop stress $-B_\phi^2/r$ would remain different from zero and artificially collimate the outflow into a beam. Such a cross-field balance numerical bias must be avoided if any serious comment on collimation is to be made. For the upper boundary of the computational domain, no pronounced reflection effects have been noticed; therefore, an outflow condition is specified for all variables. The normal component of the magnetic field is once again chosen to retain $\nabla \cdot \boldsymbol{B} = 0$. Following Ustyugova et al. (1999), we have also examined the possibility that the form of the computational domain could interfere with the collimation process due to its elongated form. Repeating some of the simulations with a different aspect ratio (i.e. with a domain spanning from 0 to $40r_0$ in the r direction and from 0 to $20r_0$ in the z-direction, resolved on to [512 × 256] cells), we found that there is minimal difference on the degree of collimation, excluding thus numerical artefacts from the rightmost boundary. This, nonetheless, does not contradict the aforementioned study, since the aspect ratio for which Ustyugova et al. (1999) found Mach cones entering the computational domain and affecting collimation was 1:4.

Given that the origin is inside the computational domain, an appropriate internal boundary must be imposed to cope with the singularity of the gravitational potential there. Moreover, the radial self-similar model is critical for $r = 0$, thus a realistic approach in that region is needed. The strategy we follow involves truncating the disc at an inner radius $r = r_0$. We set an orthogonal region [$r_0 \times 0.5r_0$] that is excluded from the computational domain and acts as a sink region emulating the central compact object. We adopt the same strategy used at the rightmost and uppermost boundary zones. The ghost cells of the internal boundary region are evaluated from the adjacent domain cells, residing either on the right (for the rightmost border of the internal boundary) or on top (for the upper border of the internal boundary) of the sink. This approach ensures smoothness of the variables' profiles during numerical calculation. Moreover, in order to ensure that no artificial outflows is allowed to exit from the internal boundary region, we impose that the poloidal velocity cannot be positive in this part of the domain.

2.4 Parameters

The model has in total seven arbitrary non-dimensional parameters. These are, using the notation adopted in the previous Section, ϵ, μ, m, α, $\chi_{\rm m}$, f and δ. The values of these parameters are subject to constrains. As seen in Ferreira (1997) in order to obtain a trans-Alfvénic solution, ϵ must have a minimum value of $\epsilon_{\rm min} = 5 \times 10^{-4}$ whereas the upper limit is defined by the thin-disc requirement, $\epsilon_{\rm max} = 0.1$. In all runs, we keep the initial value of ϵ equal to this maximum value. This is the best choice to capture the profiles of the primitive variables inside the disc. The initial bending of the field lines, dictated by m, ensures an initially force-free magnetic field at the corona and also satisfies the Blandford & Payne criterion. In this way, we can immediately reach the conditions for a magnetocentrifugally driven outflow. Thus, throughout the runs, we set $m = 0.4$. The constant δ is set 10^{-4} corresponding to a corona much lighter than the underlying accretion disc. Finally, we assume that the f function is equal to unity; we will study cold solutions by requiring that the entropy generated inside the disc (due to Ohmic heating) is radiated away, ensuring thus that the enthalpy will remain sufficiently small. Our simulations will investigate the parameter space of the other variables. The configuration we will use as reference is the one with the values used in Zanni et al. (2007) and corresponds to case 2. In Table 1, we list the six different cases studied. Cases 1–4 investigate the effect of the magnetization parameter and the need of an equipartition value for the formation of an efficient outflow, whereas cases 5 and 6 examine the effects of anisotropic resistivity for low-α configurations. Casse & Ferreira (2000a) found that in order to obtain a steady outflow solution characterized by a low α one needs anisotropy higher than 10^2.

Table 1. Parameters.

	Case 1	Case 2	Case 3	Case 4	Case 5	Case 6
μ	0.1	0.3	1.0	3.0	0.3	0.3
α	1.0	1.0	1.0	1.0	0.1	0.1
$\chi_{\rm m}$	3.0	3.0	3.0	3.0	3.0	100.0
ϵ	0.1	0.1	0.1	0.1	0.1	0.1
m	0.4	0.4	0.4	0.4	0.4	0.4
f	1.0	1.0	1.0	1.0	1.0	1.0
δ	10^{-4}	10^{-4}	10^{-4}	10^{-4}	10^{-4}	10^{-4}

Note. The choice of parameters for the six cases studied. μ is the magnetization, α the magnetic diffusivity parameter and $\chi_{\rm m}$ the anisotropy parameter for the resistivity tensor. The rest of the listed parameters [ϵ the ratio between the isothermal sound speed and the Keplerian velocity, m the parameter that controls the initial bending of the B-field (see equation 10), f the cooling function parameter and δ the corona-to-disc density ratio] are kept the same for all cases.

3 THE EFFECTS OF MAGNETIZATION

In this section, we study of the influence of the magnetic field's strength on the production, efficiency and stability of outflows in magnetized accretion–ejection structures. In Section 3.1, we discuss the impact of the variation of μ on the characteristics of the outflow, address the issue of the collimation of the magnetic field and the flow's capability to cross the critical surfaces. In Section 3.2, some remarks on the transport of angular momentum and energy will be made, as well as some comments on the outflow's ability to reach a final steady state in Section 3.3.

3.1 Outflows: velocities, acceleration and collimation

Cases 1–4 are a scan through the μ space, varying from a thermally dominated to a magnetically dominated configuration. In the analytical work of Ferreira & Pelletier (1995) and Ferreira (1997), this parameter has been well constrained. An upper limit can be found by requiring the crossing of the slow magnetosonic point. Li (1995) has shown that μ should be less than 3/4 for a set of parameters similar to ours. A lower limit on μ can also be found from the requirement of the slow surface crossing, by calculating the minimum value of the ejection index $\xi = {\rm d}\ln \dot{M}_a/{\rm d}\ln r$. In fig. 2 of Ferreira (1997), the lower limit for the ejection index corresponds to a minimum value of μ equal to 0.15 for that study. The choice of μ in cases 1,3 and 4 allows us to investigate the consequences of magnetization beyond this limit.

All simulations have been evolved up to ∼63 rotations of the inner disc radius. Due to the differential rotation, this translates into a little less than 3/4 of a revolution at $r = 20r_{\rm in}$ and ∼1/4 at the outermost

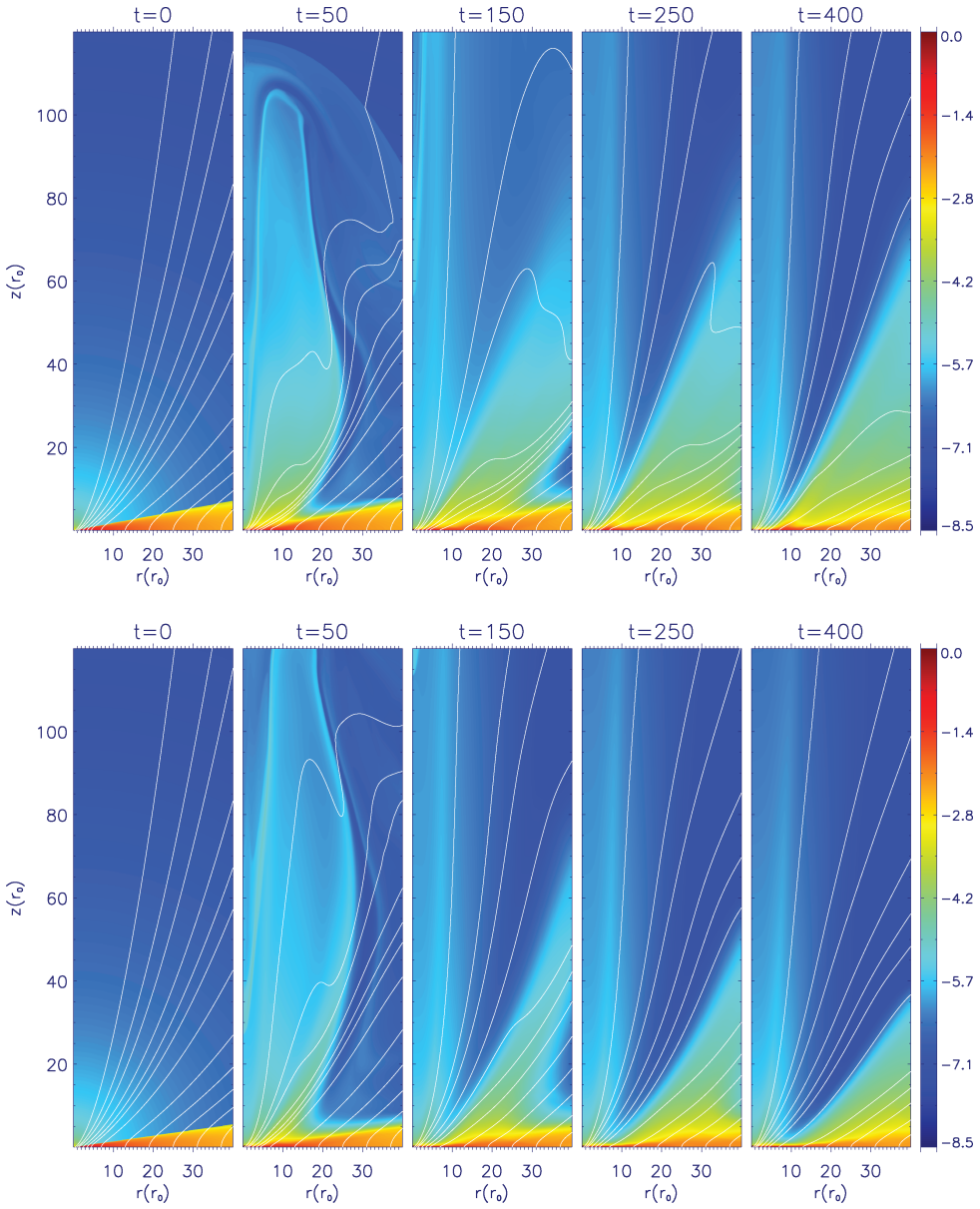

Figure 1. Evolution of logarithmic density and poloidal magnetic field for cases 1 (upper part) and 2 (lower part). The foot point of each field line is set to a same specific radius for all cases, in order to monitor the impact of magnetization in the collimation process.

part of the disc ($r = 40r_{\rm in}$). It is clear that only the innermost part of the accretion disc has performed enough revolutions so as to address stationarity.

The outflow driven from the disc varies according to the choice of magnetization. More dramatic is the evolution of the magnetic field from case to case. In Figs 1 and 2, we show the progress of the density logarithm with sample poloidal magnetic lines anchored at set foot points on the disc equator. For cases 1 and 2, we observe the formation of a light outflow from the internal region of the disc which is progressively collimated by the magnetic field; the outer part of the disc generates a dense and slow disc wind, more prominent for low magnetization. There is a difference in the time-scale of collimation but the analytically expected open-field topology is reached for both cases 1 and 2. The disc geometry does not change substantially during the evolution.

For magnetic fields above equipartition (cases 3 and 4), the field does not retain its bending but evolves into a topology almost perpendicular to the disc. This confirms analytical studies (fig. 2 in Ferreira 1997) where the increase of magnetization results in a decrease of the field's curvature. The magnetic resistivity inside the disc is larger (as specified in equation 11) whereas, as we will see later on, the accretion speed becomes smaller (Table 2) due to a weaker magnetic torque. This yields a relaxation which straightens the field lines near the base of the outflow as shown in Fig. 2 since the magnetic Reynolds number decreases and the bending is not sustained. On top of that, in the upper part of the domain there is some degree of collimation due to magnetic tension. Once the field lines straighten, the initial vertical pinch of the radial field is reduced and the thermal pressure gradient is able to load more mass on to the field lines. The magnetocentrifugal mechanism is highly inefficient in these simulations due to the small inclination of the field lines added to a strongly sub-Keplerian rotation. Also note that the accretion disc's structure is not sustained. The observed flattening is attributed to a pinch by the toroidal magnetic field at the initial

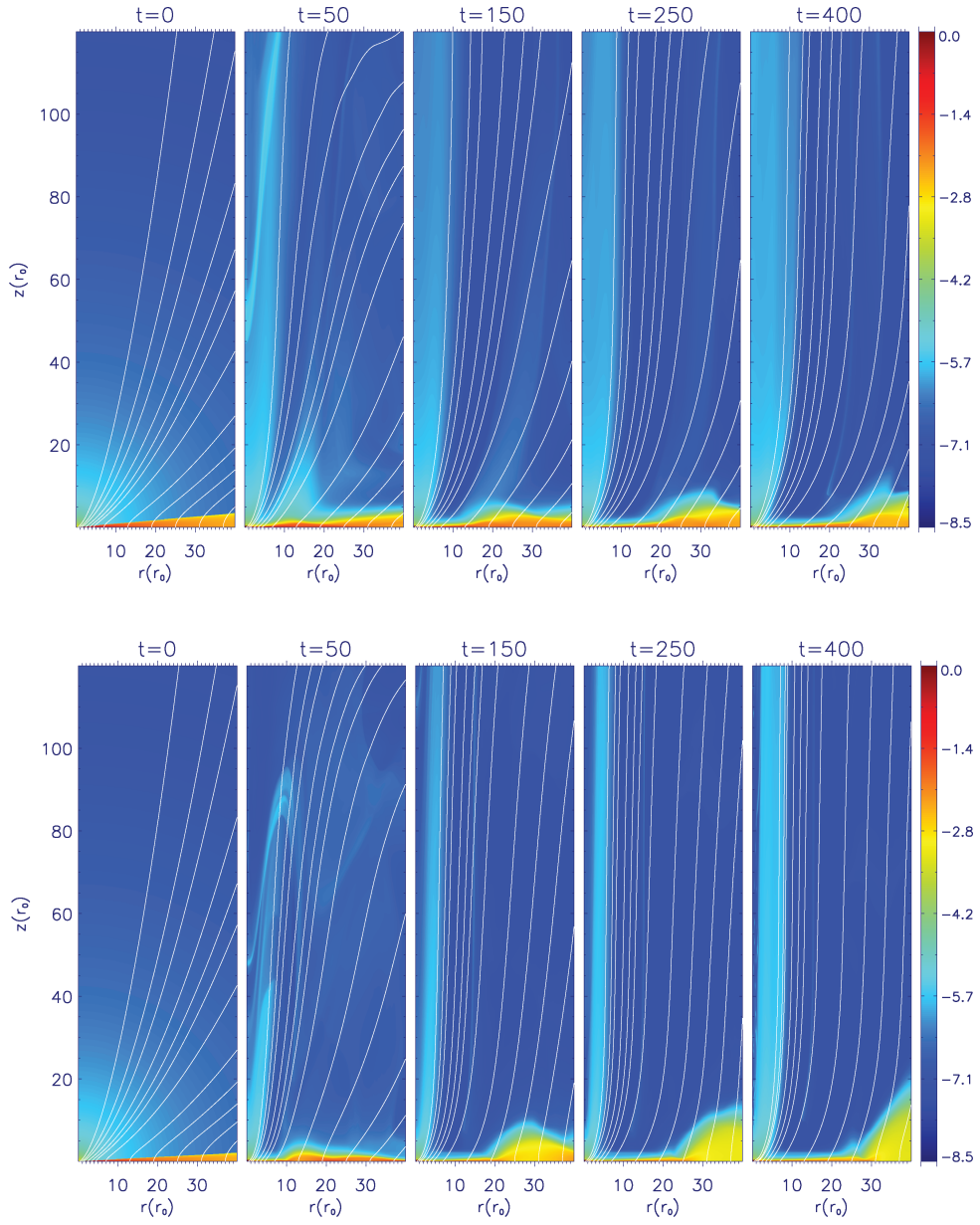

Figure 2. Same as Fig. 1 but for cases 3 (above equipartition) and 4 (high μ).

Table 2. Ejection efficiency and accretion properties.

	Plateau	$2\dot{M}_{\rm ej}/\dot{M}_{\rm acc}$	ξ	$\dot{M}_{\rm acc;e}/\dot{M}_{\rm acc;b}$	$V_{r;e}/V_{r;b}$
Case 1	Yes	∼0.06	0.027	2.12	6.1
Case 2	Yes	∼0.07	0.032	2.10	5.0
Case 3	No			1.31	4.5
Case 4	No			0.21	1.2

phases of the simulation (due to the initial azimuthal differential rotation) and the large ejection rates. It should be stressed though that both pinches (from the poloidal and the toroidal component of the magnetic field) become weaker than those of cases 1 and 2, as the simulations evolve. The absence of the outer wind is explained by the small field inclination and a deficient thermal push.

The behaviour of the magnetic lines and the acceleration of the outflow can be linked to the evolution of the poloidal current circuit. As the outflow propagates, the total current flowing within a magnetic surface (an isosurface of the magnetic flux function $A = 1/2\pi \int \boldsymbol{B}_{\rm p} \cdot {\rm d}\boldsymbol{S}$) is equal to $I = 2\pi r B_\phi$. On the poloidal plane, the current circuit follows a counterclockwise motion, moving radially outwards inside the disc, upwards in the outer part of the domain and inwards near the rotation axis. The circuit then closes in the innermost part of the accretion disc. Following Ferreira (1997), one can decompose the Lorentz force as

$$\begin{aligned} F_\phi &= \frac{B_{\rm p}}{2\pi r}\nabla_\parallel I, \\ F_\parallel &= -\frac{B_\phi}{2\pi r}\nabla_\parallel I, \\ F_\perp &= B_{\rm p} J_\phi - \frac{B_\phi}{2\pi r}\nabla_\perp I, \end{aligned} \tag{13}$$

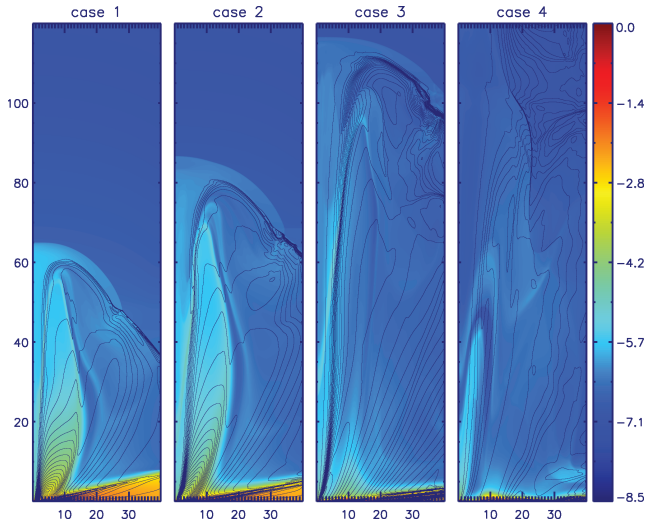

Figure 3. Four snapshots of the poloidal current distribution for the four cases studied, at time equals to 30. For values of μ below equipartition, the analytically expected butterfly topology is achieved, whereas for the magnetically dominated cases the outcome is unstable. The expansion of the initial torsional Alfvén wave is faster.

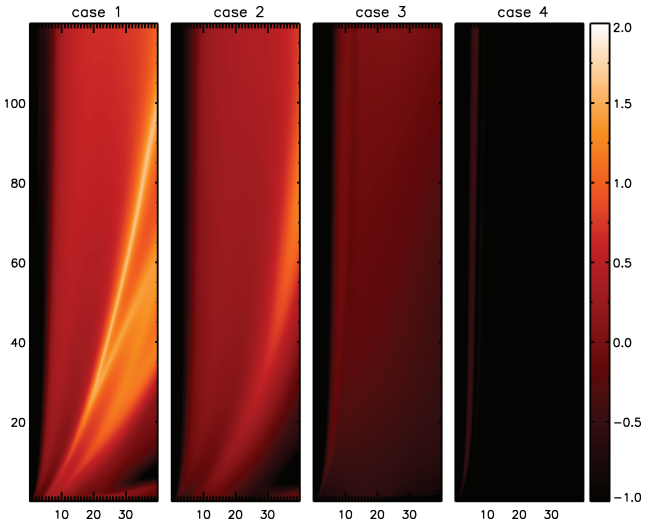

Figure 4. The logarithmic ratio of the absolute value of the toroidal magnetic field over the poloidal component at time $t = 400$.

where $\nabla_\parallel$ and $\nabla_\perp$ are derivatives along and perpendicular to the magnetic surfaces, respectively. The third equation gives the force responsible for the bending of the field.

It is clear then that the plasma is accelerated by a current leakage through the magnetic surface ($\nabla_\parallel I > 0$), giving rise to both a toroidal and a poloidal component of the Lorentz force. From the form of these equations, it becomes also evident that the poloidal force caused by the toroidal magnetic field will be perpendicular [since $F_\mathrm{p} \sim \nabla\,(rB_\phi)$] to the isocontours of the poloidal current ($rB_\phi =$ constant).

In Fig. 3, we plot the isocontours of the poloidal current for cases 1–4 at time $t = 30$. In the same figure, the propagation of the initial torsional Alfvén wave can be seen (discussed by Ustyugova et al. 1995). For values of μ below equipartition, the current circuits follow the topology described in Ferreira (1997), whereas for cases 3 and 4 the result is somewhat unstable. As the current flows anticlockwise, the poloidal component of the Lorentz force is perpendicular to the isocontours and pointing outwards. This results in the collimation of the magnetic surfaces in the inner part of the domain whereas the outer part decollimates. As the current flows radially inside the disc towards the right boundary, the Lorentz force pinches the disc. As shown in equation (13), the two components of the Lorentz force responsible for the magnetic acceleration are F_p and F_ϕ. To define which is dominant, we evaluate their ratio

$$\frac{F_\parallel}{F_\phi} = -\frac{B_\phi}{B_\mathrm{p}}. \tag{14}$$

Since in our simulations $B_\phi < 0$, equation (14) shows that for the region where the toroidal magnetic field is greater than the poloidal one ($B_\phi/B_\mathrm{p} > 1$), the acceleration is mainly poloidal. On the other hand, Fig. 4 shows that there are regions where the ratio is less than unity and the toroidal acceleration is more important. The magnetocentrifugal mechanism can usually be seen as a two-phase process: near the disc's surface and below the Alfvén radius (the poloidal velocity is smaller than the Alfvén speed; cf. equation 15), the magnetic field is strong enough to impose the corotation of the outflowing plasma with the field lines ($B_\phi \ll B_\mathrm{p}$). Above the Alfvén surface, corotation stops and due to inertia the plasma lags behind, while the field gets wound up ($B_\phi \gg B_\mathrm{p}$). For a complete description of the mechanism see Blandford & Payne (1982). This, combined with the argument of equation (14), simply shows that in the corotation regime the poloidal force is less important than the toroidal one. The latter provides the 'centrifugal' acceleration that in fact constitutes the mechanism more of a magnetically driven one than a centrifugally driven (Lovelace, Berk & Contopoulos 1991; Contopoulos & Lovelace 1994). Above the Alfvén surface, the poloidal acceleration dominates. Since the magnetic tension poloidal component is not so important at those heights, the main driving force is the gradient of the magnetic pressure (of B_ϕ).

The magnetization parameter, by controlling the strength of the field, is important in defining which phase prevails (Fig. 4). For weakly magnetized outflows, the toroidal acceleration prevails in the sub-Alfvénic region and since the field lines are sufficiently inclined the centrifugal force accelerates the outflow. In the super-Alfvénic region, F_p prevails and provides some residual acceleration, even if a great part of the acceleration has taken place in the sub-Alfvénic region. For magnetically dominated configurations, the poloidal component of the Lorentz force is almost never a significant factor, compared to the toroidal one. As already pointed out, the largely sub-Keplerian disc corotates with the almost straight magnetic field lines characterized by a negligible twisting: a faint acceleration can happen because of thermal pressure gradients and a weak magnetic force. Moreover, the small B_ϕ/B_p ratio indicates that, despite the higher poloidal field strength, the magnetic torque is weaker than in the low-μ cases: this determines a slower accretion speed, a smaller accretion rate and a reduced magnetic Reynolds number which favours the outward diffusion of the field lines and decreases the bending.

The reason behind this is that, due to the magnetic torque and the strong coupling with the corona, the disc is magnetically braked more efficiently in the initial phases for high-μ cases, when there is a prominent differential rotation between the disc and the corona. In the advanced states, this differential rotation is almost zero, as confirmed by the fact that B_ϕ/B_p takes really small values. This yields an angular momentum redistribution in the initial phases, that is amplified by the ejection's torque. All these factors produce a toroidal component of the magnetic field with weak poloidal

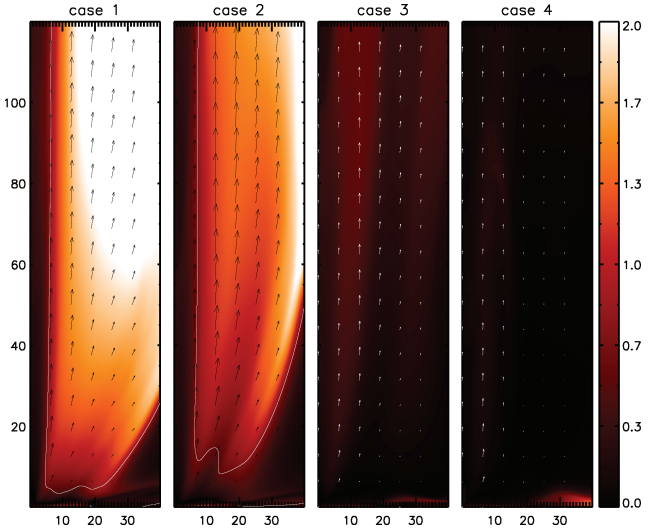

Figure 5. The effect of magnetization on the ability of the outflow to cross the critical surfaces. The figure displays snapshots at $t = 200$ of the poloidal velocity over the fast magnetosonic. The solid line indicates the Alfvénic surface and the poloidal velocity vectors are overimposed. The length of the arrows is normalized to the maximum poloidal speed reached in case 1. The position of the Alfvénic surface is closer to the disc as μ decreases.

gradients, and the toroidal component of the Lorentz force is the dominant one.

Regarding the efficiency of the acceleration in each case, we can examine how solutions cross the critical surfaces, i.e. the isosurfaces where the poloidal velocity component becomes equal to one of the three MHD wave speeds:

$$V_{\rm Ap}^2 = \frac{{B_{\rm p}}^2}{\rho},$$

$$V_{\rm fm,sm}^2 = \frac{\left(C_{\rm s}^2 + V_{\rm A}^2\right) \pm \sqrt{\left(C_{\rm s}^2 + V_{\rm A}^2\right)^2 - 4C_{\rm s}^2 V_{\rm Ap}^2}}{2}, \qquad (15)$$

where $V_{\rm A}^2 = B^2/\rho$ is the total Alfvénic speed and $C_{\rm s} = \sqrt{\gamma P/\rho}$ is the sound velocity. Only solutions crossing these critical points produce steady outflows. In Fig. 5, we display the ratio of the poloidal over the fast magnetosonic velocity. The solid line is the Alfvénic surface, while vectors depict the poloidal flow lines.

Clearly, the flow crosses the Alfvénic surface inside our domain only for magnetization values below equipartition (i.e. cases 1 and 2). Moreover, the position of the Alfvén's surface is closer to the disc as μ decreases. In cases 3 and 4, we can see that the outflow fails to become super-Alfvénic. That does not necessarily mean that the outflow will not eventually reach such velocities for a larger computational domain and therefore far away from the disc. It should be stressed, nonetheless, that both the magnetic surface inclination (unavoidably violating the BP criterion and not promoting the conversion of magnetic to kinetic energy discussed later on) and the slower rotation do not favour an efficient acceleration through a magnetocentrifugal mechanism. The Alfvén and fast critical surfaces can only be crossed (by the whole spread of the outflow) by cases 1 and 2 for which magnetization is below equipartition. The remaining two cases are either subfast (case 3) or even mostly subslow (case 4).

In order to clarify which driving force is responsible for the acceleration, we display for case 2 the forces acting *along* a reference field line (Fig. 6, upper panel). It is clear that the main accelerating force is the centrifugal in the sub-Alfvénic region, while as

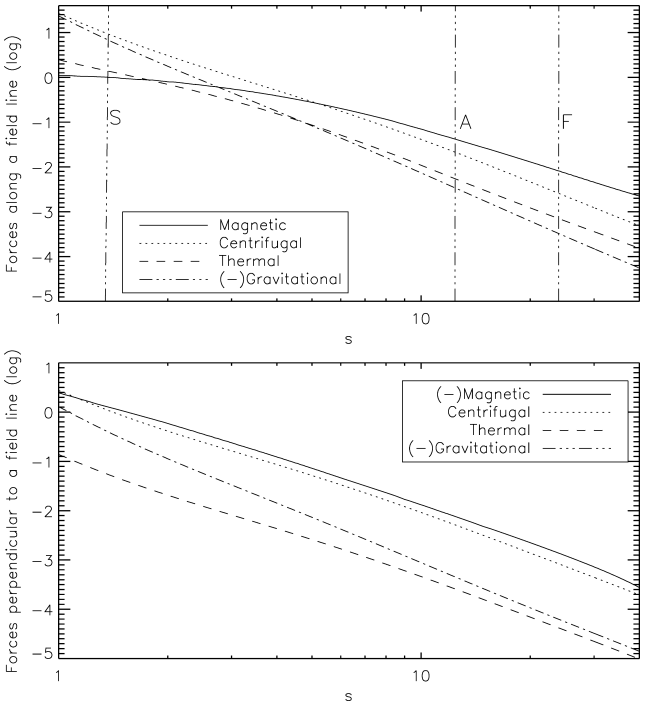

Figure 6. Upper panel: logarithmic magnitude of forces *along* a field line with its foot point anchored at $R = 1.5$ at time $t = 400$ for case 2. Displayed are the Lorentz (solid line), centrifugal (dotted line), thermal (dashed line) and gravitational (dot–dashed line) forces. Forces that in the legend display a (–) in front decelerate the outflow. The letters S, A and F are used to denote the critical points, respectively, the slow magnetosonic, Alfvén and fast magnetosonic. Lower panel: logarithmic magnitude of forces *perpendicular* to the same field line. Forces that in the legend display a (–) in front collimate the outflow.

the critical Alfvén point is reached the Lorentz force dominates (in agreement with Lovelace et al. 1991; Ferreira 1997; Ustyugova et al. 1999). Thermal pressure gradients are not important as far as the outflow's drive is concerned while gravity matters only below the slow point.

On the other hand, the projection of forces *perpendicular* to the field line can give insightful information on the collimation process. As seen in the lower panel of Fig. 6, the collimation is mainly due to the magnetic force that tends to be balanced out by the decollimating centrifugal one, as occurs for current-carrying outflows (Ferreira 1997; Casse & Ferreira 2000a). Once again, thermal and gravitational forces are not so important for the decollimation/collimation process, respectively.

3.2 Outflows: ejection efficiency, angular momentum transport and energetics

Here, we examine the impact of the magnetic field strength on the rates of accretion and ejection. The very essence of the coupling of the accretion disc with the outflow is the transfer of energy and angular momentum. In order to quantify these rates, it is convenient to introduce a control volume, where to compute the values of these quantities. We use the form of a disc sector with two surfaces S_i and S_e perpendicular to the equator of the disc at $r_i = 1$ and $r_e = 10$ and height $2H(r_i)$ and $2H(r_e)$, respectively. The inclined surface on top of the disc, through which we calculate the ejection rates, will be denoted as $S_{\rm d}$.

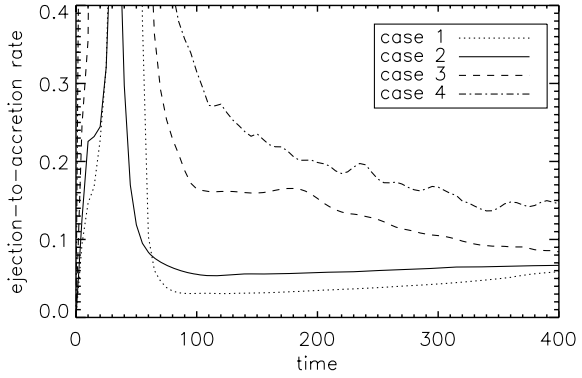

Figure 7. Mass ejection-to-accretion rates as a function of time, taking into consideration jet and counter jet. The notation used is: case 1 dotted; case 2 solid; case 3 dashed and case 4 dot–dashed lines. The trend shows an increase of the ratio as the magnetic field becomes stronger. Cases 3 and 4 decay into smaller values though as the ejection is not sustained. These two cases do not reach a steady configuration in contrast to the clear plateau reached for low-magnetization configurations.

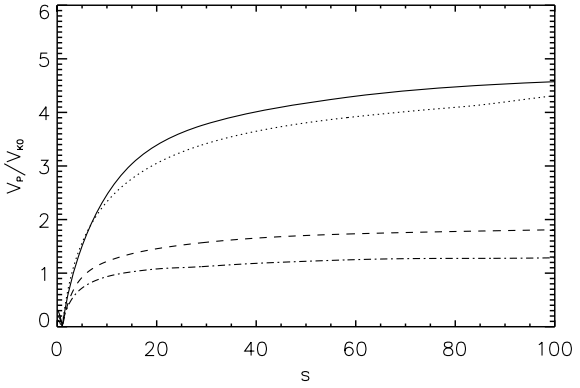

Figure 8. Poloidal velocity along a field line with foot point anchored at $R = 1.5$ and normalized over the keplerian speed at the foot point at time $t = 400$. Following the trend of ξ, the low ejection rates are accelerated more efficiently. The notation is the same as Fig. 7.

The mass flux entering the control volume from the S_e surface is given by the following integral:

$$\dot{M}_{\rm acc} = -2\pi r \int_{-2H}^{2H} \rho u_r \, {\rm d}z, \tag{16}$$

whereas the mass ejected through the $S_{\rm d}$ surface can be found by a similar expression, namely

$$\dot{M}_{\rm ej} = \int_{S_{\rm d}} \rho \boldsymbol{u} \cdot {\rm d}\boldsymbol{S}. \tag{17}$$

Note that the accretion rate calculated in this way takes into account both halves of the disc, taking advantage of the equatorial symmetry assumption for density and radial velocity. Conversely, the ejection rate of equation (17) includes only one of the jet beams (without considering the counterjet).

In Fig. 7, we plot $2\dot{M}_{\rm ej}/\dot{M}_{\rm acc}$, the ratio of the ejection to accretion flux including both jet and counterjet, as a function of time for all four cases. This ejection efficiency $2\dot{M}_{\rm ej}/\dot{M}_{\rm acc}$ settles to higher values as the magnetization increases. A clear plateau is reached for cases 1 and 2 after the initial transient phase, an indication of a stationary solution. In cases 3 and 4, the ejection efficiency instead oscillates towards smaller values. This is a clear evidence that for strong magnetic fields, a sustained acceleration is not achieved and a stationary solution is not found. Table 2 summarizes these results.

In terms of the ejection index ξ, which was previously defined as $\xi = {\rm d}\ln \dot{M}_{\rm acc}/{\rm d}\ln r$, mass conservation in the control volume yields

$$\frac{2\dot{M}_{\rm ej}}{\dot{M}_{\rm acc}} = 1 - \left(\frac{r_i}{r_e}\right)^{\xi}. \tag{18}$$

From equation (18), it is clear that as the ejection efficiency increases so does the index. In accordance with analytical results (see Ferreira 1997, fig. 2), an increase in μ is accompanied by a gain in the ejection index ξ. Note, however, that the analytical parameter space is quite narrow and does not encompass cases 1, 3 and 4 of our study. Also in agreement with the aforementioned study, due to the inefficiency of the magnetic acceleration, solutions with high ejection rates and large magnetizations do not allow super-Alfvénic outflows (Blandford & Payne 1982; Wardle & Königl 1993; Ferreira 1997).These results, coupled with Fig. 4, might at first seem contradictory to the conclusion of Zanni et al. (2007) that the elevated values of the ejection index yield further bending of the field lines and make the magnetic pressure acceleration mechanism dominant. Indeed, this holds true for configurations of the same magnetization but different ejection indices and resistivities. None the less, for magnetically dominated configurations the initial equilibrium requirement of the disc and the stronger braking correspond to a slower rotation. In turn, this leads to a comparatively weaker toroidal magnetic field gradients and a curvature of the field line that favour corotation. The last two columns of Table 2 indeed show that both the accretion rate and the accretion velocity (mean value of u_r inside the control volume) decrease as μ increases, further lowering the magnetic Reynolds number.

One more aspect to note comparing cases 1 and 2 is the Alfvén's surface azimuthal distance from the disc (shown previously in Fig. 5), which is smaller for lower values of magnetization (and subsequently of ξ). This has also been observed in analytical results (see fig. 4 of Ferreira 1997) and can be explained by the large energy required for accelerating strong ejections up to the Alfvénic critical point.

To quantify the terminal velocity reached for each case, we calculate the poloidal speed of the flow along a reference inner magnetic field line. Fig. 8 shows that in order to have efficient acceleration (depicted is the poloidal velocity normalized to the Keplerian one at the foot point of the line) low-magnetization configurations are needed. Also note that a substantial part of the acceleration takes place in the sub-Alfvénic region of the domain, near the outflow's base, while it saturates at $s \sim 40$. Since the field line chosen coincides with the one of Fig. 6, we can see that for the acceleration of the flow, from 0 to $\sim$2 $V_{\rm K0}$, the centrifugal force is responsible, whereas the poloidal component of the Lorentz force provides the drive from 2 to $\sim$4.5 $V_{\rm K0}$.

Another way to evaluate the efficiency of the acceleration mechanism is the transformation of the Poynting flux to kinetic energy along a magnetic field line. Parametrizing this ratio with

$$\sigma = \frac{-2\Omega r B_\phi B_{\rm p}}{\rho u^2 u_{\rm p}}, \tag{19}$$

we have a measure of the energy stored as magnetic energy relative to the kinetic energy. Ω denotes the rotation rate of the magnetic surface. At the base of the outflow, σ is proportional to the injection of energy into jets. According to the Blandford & Payne acceleration model, this ratio should take small values at the super-Alfvénic region.

As shown in Fig. 9, the available energy for the acceleration is larger for low-μ configurations, in agreement with the trend of the

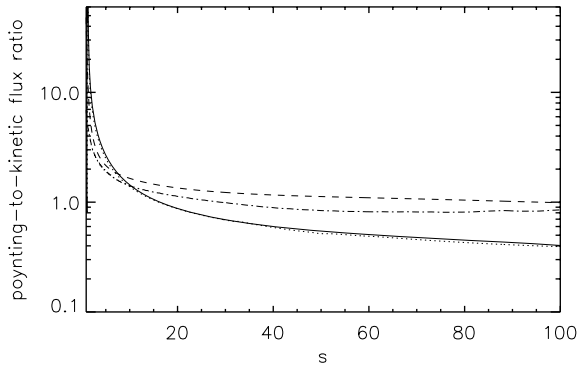

Figure 9. Poynting-to-kinetic flux along a field line anchored at $R = 1.5$. The notation is the same as Fig. 7.

ejection index (as $\sigma \sim 1/\xi$ at the outflows base). On top of that, the transformation rate for strongly magnetized cases is far slower, implying that a substantial part of the magnetic energy at the upper part of our domain is yet to be transformed into kinetic, which means that we have not reached an asymptotic solution. It is actually likely though that since the magnetic surfaces are cylinders the conversion will stop there. These results fit well with the observed velocities (Fig. 8). From radial cuts in the upper end of the domain, the mean value of σ for cases 1 and 2 is of the order of 2–4 $\times$ 10^{-1} whereas for cases 3 and 4 lies between 3 and 4.

Another issue to investigate is the transport of angular momentum from the accretion disc to the outflow. In order to quantify this value, we take advantage once more of the control volume defined above and compute the balance of angular momentum flux as follows:

$$\begin{aligned}
\dot{J}_{\rm acc,kin} &= \int_{S_i} r_i \rho u_\phi \boldsymbol{u} \cdot {\rm d}\boldsymbol{S} - \int_{S_{\rm e}} {\rm r_e} \rho {\rm u}_\phi \boldsymbol{u} \cdot {\rm d}\boldsymbol{S}, \\
\dot{J}_{\rm acc,mag} &= \int_{S_i} r_i B_\phi \boldsymbol{B} \cdot {\rm d}\boldsymbol{S} - \int_{S_{\rm e}} {\rm r_e B}_\phi \boldsymbol{B} \cdot {\rm d}\boldsymbol{S}, \\
\dot{J}_{\rm acc} &= \dot{J}_{\rm acc,kin} + \dot{J}_{\rm acc,mag}.
\end{aligned} \tag{20}$$

The accretion torque $\dot{J}_{\rm acc}$ takes positive sign if it increases the angular momentum of the control volume. Accordingly, we can define an ejection torque that is the torque exerted on the disc by the outflow:

$$\begin{aligned}
\dot{J}_{\rm jet,kin} &= \int_{S_{\rm d}} r \rho u_\phi \boldsymbol{u} \cdot {\rm d}\boldsymbol{S}, \\
\dot{J}_{\rm jet,mag} &= \int_{S_{\rm d}} r B_\phi \boldsymbol{B} \cdot {\rm d}\boldsymbol{S}, \\
\dot{J}_{\rm jet} &= \dot{J}_{\rm jet,kin} + \dot{J}_{\rm jet,mag}.
\end{aligned} \tag{21}$$

A positive sign means that the torque extracts angular momentum from the control volume.

Table 3 shows that the ratio $2\dot{J}_{\rm jet}/\dot{J}_{\rm acc}$ has an approximate value of unity, which means that angular momentum is conserved within the control volume. The second column shows that the greatest part of angular momentum extraction is attributed to the magnetic torque at the base of the outflow. Moreover, the magnetic torque of the disc (column 3) reduces the angular momentum, further favouring accretion. Its role, however, is small compared to the torque exerted by the outflow. The data of the fourth column show that for case 2 we have also the most efficient extraction: only a 19 per cent of the angular momentum flux that crosses the outer border of the control volume reaches the inner side. The value of the angular momentum stored in the magnetic field at the base of the outflow is important for an estimate of the efficiency of acceleration through the magneto-centrifugal mechanism and in all cases the $\dot{J}_{\rm jet\ mag}$ component is more than the 85 per cent of the total angular momentum extracted. On the basis of the trend shown in Table 3, we can expect higher velocities for the low-μ cases, as illustrated in Fig. 8.

The energy budget of the system can be addressed in a similar manner as the angular momentum transport. The energy fluxes of the accretion process can be defined as

$$\begin{aligned}
\dot{E}_{\rm acc,grv} &= \int_{S_i} \Phi_{\rm g} \rho \boldsymbol{u} \cdot {\rm d}\boldsymbol{S} - \int_{S_{\rm e}} \Phi_{\rm g} \rho \boldsymbol{u} \cdot {\rm d}\boldsymbol{S}, \\
\dot{E}_{\rm acc,kin} &= \int_{S_i} \frac{1}{2} u^2 \rho \boldsymbol{u} \cdot {\rm d}\boldsymbol{S} - \int_{S_{\rm e}} \frac{1}{2} {\rm u}^2 \rho \boldsymbol{u} \cdot {\rm d}\boldsymbol{S}, \\
\dot{E}_{\rm acc,mag} &= \int_{S_i} \boldsymbol{E} \times \boldsymbol{B} \cdot {\rm d}\boldsymbol{S} - \int_{S_{\rm e}} \boldsymbol{E} \times \boldsymbol{B} \cdot {\rm d}\boldsymbol{S}, \\
\dot{E}_{\rm acc,thm} &= \int_{S_i} \frac{\gamma}{\gamma - 1} P \boldsymbol{u} \cdot {\rm d}\boldsymbol{S} - \int_{S_{\rm e}} \frac{\gamma}{\gamma - 1} {\rm P} \boldsymbol{u} \cdot {\rm d}\boldsymbol{S}, \\
\dot{E}_{\rm acc} &= \dot{E}_{\rm acc,grv} + \dot{E}_{\rm acc,kin} + \dot{E}_{\rm acc,mag} + \dot{E}_{\rm acc,thm},
\end{aligned} \tag{22}$$

where once again a positive sign corresponds to an increase in the energy inside the control volume. The same approach for the outflow will read

$$\begin{aligned}
\dot{E}_{\rm jet,grv} &= \int_{S_{\rm d}} \Phi_{\rm g} \rho \boldsymbol{u} \cdot {\rm d}\boldsymbol{S}, \\
\dot{E}_{\rm jet,kin} &= \int_{S_{\rm d}} \frac{1}{2} u^2 \rho \boldsymbol{u} \cdot {\rm d}\boldsymbol{S}, \\
\dot{E}_{\rm jet,mag} &= \int_{S_{\rm d}} \boldsymbol{E} \times \boldsymbol{B} \cdot {\rm d}\boldsymbol{S}, \\
\dot{E}_{\rm jet,thm} &= \int_{S_{\rm d}} \frac{\gamma}{\gamma - 1} P \boldsymbol{u} \cdot {\rm d}\boldsymbol{S}, \\
\dot{E}_{\rm jet} &= \dot{E}_{\rm jet,grv} + \dot{E}_{\rm jet,kin} + \dot{E}_{\rm jet,mag} + \dot{E}_{\rm jet,thm}.
\end{aligned} \tag{23}$$

Table 3 illustrates how magnetization affects the magnetic component of both accretion and ejection power. As seen from the fifth column, the energy is conserved. The σ parameter, discussed earlier, is equal to the ratio $\dot{E}_{\rm jet,mag}/\dot{E}_{\rm jet,kin}$. As shown in the sixth column, the magnetic power stored in the field which is responsible for the acceleration of the outflow becomes smaller than the kinetic energy flux as the value of μ exceeds equipartition. Both accretion and ejection enthalpy powers (columns 7 and 8) increase with μ. This phenomenon could be linked to numerical dissipation on the disc surface which we discuss later on.

Table 3. Angular momentum transport and energy budget.

	$2\dot{J}_{\rm jet}/\dot{J}_{\rm acc}$	$\dot{J}_{\rm jet;mag}/\dot{J}_{\rm jet}$	$\dot{J}_{\rm acc\ mag}/\dot{J}_{\rm acc}$	$\dot{J}_{\rm acc\ i}/\dot{J}_{\rm acc\ e}$	$2\dot{E}_{\rm jet}/\dot{E}_{\rm acc}$	σ	$\dot{E}_{\rm acc\ thm}/\dot{E}_{\rm acc}$	$\dot{E}_{\rm jet\ thm}/\dot{E}_{\rm jet}$
Case 1	0.94	0.95	−0.15	0.25	1.00	∼31	−0.003	0.01
Case 2	1.00	0.94	−0.12	0.19	0.91	∼28	−0.006	0.02
Case 3	1.00	0.91	−0.14	0.22	0.92	∼15	−0.042	0.10
Case 4	0.93	0.85	−0.03	0.26	0.90	∼7	−0.063	0.14

3.3 Reaching a steady-state configuration

We now study the ability of the four configurations of magnetization to reach a steady state. A first hint can already be found in Fig. 7 where the ejection to accretion rate allows us to estimate the relaxation of the system. Only for cases 1 and 2, corresponding to magnetization values of the analytical solutions, a steady plateau is reached. For the strongly magnetized cases 3 and 4, the outcome is not stationary as it continues to decay slowly and irregularly.

Apart from this qualitative estimate, we can monitor the evolution of solutions towards steady-state configurations following the behaviour of the integral quantities that MHD axisymmetric analytical models have shown must be conserved along any given magnetic surface in steady-state configurations (Tsinganos 1982). In terms of the quantity $A = 1/2\pi \int \boldsymbol{B}_{\rm p} \cdot {\rm d}\boldsymbol{S}$, i.e. the poloidal magnetic flux of a field line whose foot point is situated at r_0, we can write the following integrals:

$$\begin{aligned}
\Psi(A) &= \sqrt{4\pi}\rho \frac{V_{\rm p}}{B_{\rm p}}, \\
\Omega(A) &= \frac{1}{r}\left[V_\phi - \frac{\Psi(A) B_\phi}{\sqrt{4\pi}\rho}\right], \\
L(A) &= r\left[V_\phi - \frac{\sqrt{4\pi}B_\phi}{\Psi(A)}\right],
\end{aligned} \tag{24}$$

where $\Psi(A)$ is the mass-to-magnetic flux ratio; the reader should keep in mind that $1/\sqrt{4\pi}$ is encompassed within the magnetic field in the code's normalization – see equation (2), $\Omega(A)$ is the rotation rate of the magnetic surface and $L(A)$ is the specific angular momentum shared between the flow component and the magnetic field. In addition, we have energy integrals of motion that for a cold configuration of a polytropic index γ are

$$\begin{aligned}
E(A) &= \frac{V^2}{2} + \frac{\gamma}{\gamma - 1}\frac{P}{\rho} + \Phi - r_0 \Omega(A) \frac{\sqrt{4\pi}B_\phi}{\Psi(A)}, \\
Q(A) &= \frac{P}{\rho^\gamma},
\end{aligned} \tag{25}$$

where $E(A)$ denotes the total energy-to-mass flux density and $Q(A)$ the specific entropy.

Fig. 10 displays the values of these integrals as a function of position s along the field line at some advanced stage. We use a sample field line rooted in the innermost part of the ejection region at a radius $1.5R_{\rm in}$ and plot the quantities at $t = 400$. The integrals are constant for low-magnetization cases. Conversely, deviations from stationary state arise for cases 3 and 4 as the angular momentum and the mass-to-magnetic flux ratio are clearly not conserved for these particular cases. From the rotation rate (upper-left panel), it is quite evident that as magnetization increases the rotation rate decreases, due to a stronger braking. This in fact explains why for strong magnetic fields, even though toroidal acceleration is dominant, we do not achieve high terminal velocities: the available angular momentum (upper-right panel) is less as compared to that for smaller values of μ. Moreover, the available energy is once again higher for cases 1 and 2, whereas the end value of the conserved variable is reached at shorter heights.

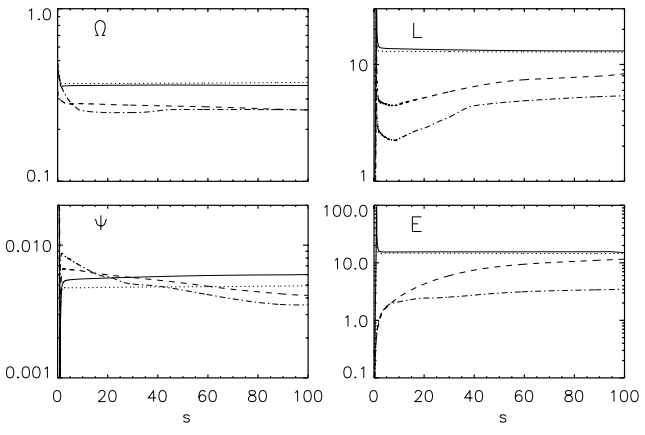

Figure 10. The first four MHD integrals of motion for all cases. The notation used is the same as in Fig. 7.

Another interesting quantity worth measuring is the magnetic lever arm, defined at the Alfvénic surface as

$$\lambda = \frac{L(A)}{\Omega(A) r_0^2} = \left(\frac{r_{\rm A}}{r_0}\right)^2. \tag{26}$$

Its value also must be conserved along the magnetic field line. For case 1, we calculate a lever arm of $\sim$14, whereas for case 2 we find a λ of the order of $\sim$16. This calculation refers to the field line chosen for the computation of the integrals shown in Fig. 10. A more careful calculation though mediating the lever arm from different radii (1.5, 2.5, 3.5, 4.5 $r_{\rm in}$) shows a different trend. For case 1, we find $\lambda \sim 19.5$ and case 2 $\lambda \sim 17.5$, which are more consistent with the formula $\lambda \sim 1 + 1/2\xi$ of Ferreira (1997). Since our calculations of ξ are done utilizing an extended control volume (discussed earlier), the second set of values is more precise. For cases of magnetization above equipartition, this value is nonsensical due to their failure to properly cross the Alfvénic surface. As the magnetization increases we saw that the ejection index increases accordingly. The inverse happens for the specific angular momentum and lever arm, as ξ is analogous to the mass load, an increase of which results to lower L (confirming Blandford & Payne 1982; Ouyed & Pudritz 1997; Ferreira 1997).

In conclusion, cases 1 and 2 reach a reasonably stationary state, while cases 3 and certainly 4 cannot be described as a steady configuration. This statement applies of course only to the innermost part of the magnetized disc, i.e. the ejection region. The outer part, even for magnetization below equipartition, has not been allowed to evolve for an adequate number of revolutions to reach stability ($\sim$1/4 rotations at $r = 40r_{\rm in}$). None the less, since both the jet torque and power evolve, although the ratio ejection-to-accretion stabilizes (see Table 3), we can deduce that the system evolves through a series of quasi-stationary states as described in Zanni et al. (2007).

At this point, we wish to focus on some comparisons of global accretion–ejection simulations that include the accretion disc consistently with analytical solutions of adiabatically expanding outflows (Ferreira 1997; Casse & Ferreira 2000a). Simulations typically yield smaller magnetic lever arms and terminal velocities, as well as larger values of ejection indices. Namely, for a configuration close to case 2 Ferreira (1997) would expect $\xi \sim 10^{-2}$, $\kappa \sim 2\,10^{-2}$ and $\lambda \sim 35$ with a terminal velocity of $V_{\rm p\infty} = \Omega r_0 \sqrt{2\lambda - 3} \sim 8.2 V_{\rm K}$, while in our case we found $\xi \sim 3\ 10^{-2}$, $\kappa \sim 4\,10^{-2}$, $\lambda \sim 16$ and a terminal velocity of only $\sim$4.5 $V_{\rm K}$. Even though such a configuration falls into the stable branch of the solutions found in Königl (2004), there is a deviation from the analytical expectations of Ferreira (1997). This could be attributed to some numerical effects, brought in by the returning current sheet which closes the current circuit inside the disc and the numerical dissipation on the disc surface, as we discuss below. It should be stated though that our results are much closer to the analytical estimates if compared to previous studies (Casse & Keppens 2002, 2004; Zanni et al. 2007).

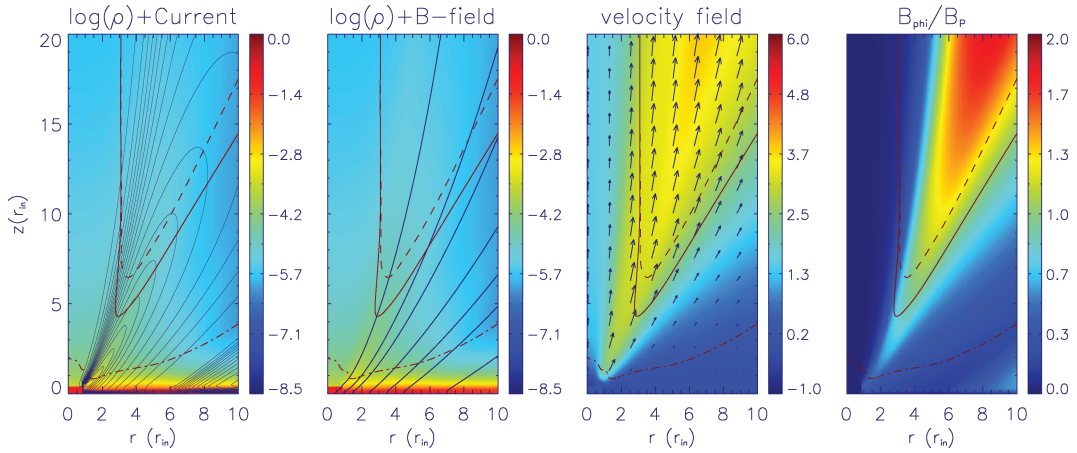

Figure 11. A closeup for the ejection region in case 2 after ∼63 rotations of the inner disc radius. From left to right are depicted the poloidal current circuit, sample magnetic field lines, velocity vectors and the absolute value of the toroidal-to-poloidal magnetic field ratio. Displayed are also the conical critical surfaces, denoted as a dash–dotted line for the slow magnetosonic, solid for the Alfvén and dashed for the fast magnetosonic. Note how the current circuit does not close on the central object but on the innermost part of the disc. The resulting field topology is open and velocity vectors are well aligned with the field lines. Moreover, the locus of the Alfvén surface is where the ratio B_ϕ/B_p equals to unity.

Return current sheet. As shown in Fig. 11, the current circuit closes inside the disc at the innermost part of the ejection region, i.e. at a radius ~ 1–$1.5r_\mathrm{in}$. As already suggested in Ferreira (1997) and Zanni et al. (2007), this results in an increase of the ejection index even though it is not as prominent as it would be for a more extensive current sheet (unsteady cases with $\xi > 0.5$). The Lorentz force associated with the toroidal field pushes up the material at the disc surface instead of pinching the disc, increasing ξ. Contrary to previous works in our simulations, the current closes much closer (if not inside) to the inner boundary.

In order to overcome this numerical effect, that stems from the existence of a non-rotating internal boundary, one should treat that region either with a two-component approach (Meliani et al. 2006; Matsakos et al. 2007), a stellar wind and a disc wind so that the current sheet can interact with a stellar wind component (closing on to the star region) or with a correct treatment of the central object in the star–disc interaction approach (Bessolaz et al. 2008; Romanova, Kulkarni & Lovelace 2008). Obviously, this would require large computational resources and adaptive grid techniques due to the scale difference.

Numerical dissipation on the disc's surface. The effects of numerical dissipation can be seen in the entropy profiles (Fig. 12).

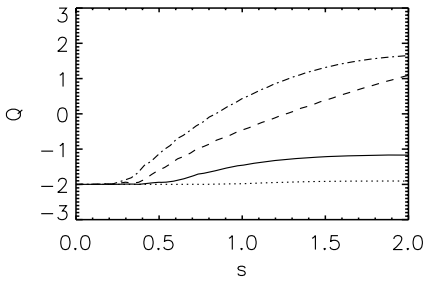

Figure 12. Specific entropy along a magnetic field line for the four cases. The notation used is the same as in Fig. 7. The foot point in this case is anchored at a radius $r = 5r_\mathrm{in}$ to better display the numerical dissipation in the base of the outflow, since for geometrically thicker part of the disc the effect is less pronounced but spread in greater heights. Since numerical resistivity interferes with the energy equation the heating is more prominent for higher values of magnetization.

The analytical models for adiabatic expansion have an extremely steep density profile at the disc surface, which within a few thermal height scales drop by five or six orders of magnitude (see fig. 8 in Ferreira 1997). Such a jump cannot be treated by present numerical codes. This results in a region at the disc surface that dissipates and heats numerically the outflow at its base. This is why in all our simulations the density profiles are comparatively smoother than the analytical results. In fact, when compared to the warm solutions (fig. 8 in Casse & Ferreira 2000b) the density profiles fit better. The same holds for parameters as the lever arm and the ejection index. For warm solutions, smaller values of λ are expected than in the adiabatic case whereas the observed ξ are higher, as heating promotes massive outflows.

Finally, we want to discuss the case of low magnetization, i.e. case 1. Even though the field topology corresponds to a borderline quasi-steady configuration, the outflow solutions cross the critical surfaces and reach acceptable terminal velocity values. Two more test cases have been studied in the ambient of even weaker magnetic fields (magnetization values of $\mu = 10^{-2}$ and 10^{-3}). The results are highly unsteady, with the open field behaving kinematically. Moreover, the maximum values of velocities reached by the weak wind are considerably less than those of case 2, reaching as low as $0.2V_\mathrm{K}$ for $\mu = 10^{-3}$. The current circuit in those cases, even though somewhat ordered, does not assume the butterfly configuration. The pressure gradient is insufficient to drive high terminal velocities. In any case, a proper treatment would essentially require the introduction of a physical viscosity since for magnetization lower than 0.1 the viscous torque becomes important. For low magnetizations, cold jets cannot be launched as, in order to keep a high magnetic torque, a strong magnetic shear q is needed that would vertically crush the disc. In order to obtain accretion, we must encompass a different angular momentum transport mechanism, i.e. turbulent viscosity.

4 RESISTIVITY ANISOTROPY

We now examine the remaining two cases calculated (5 and 6), which correspond to high anisotropy, small diffusivity configurations. As shown in Casse & Ferreira (2000a), a necessary condition to launch a cold jet is that the ratio of magnetic to viscous torque Λ

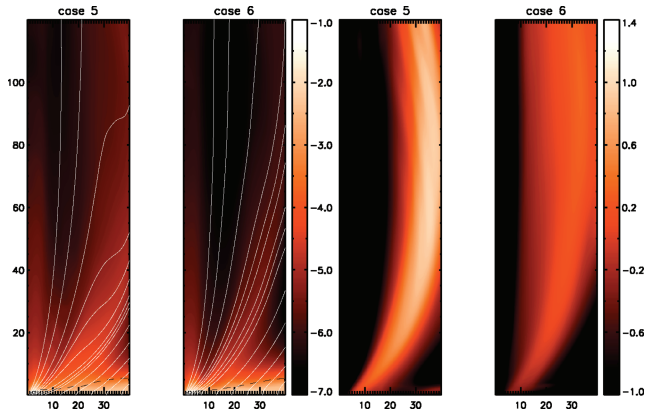

Figure 13. The first two images on the left represent the logarithmic density with sample field lines for cases 5 (low diffusivity) and 6 (low diffusivity and high anisotropy). The last two on the right depict the logarithmic ratio of the toroidal-to-poloidal magnetic field component. These snapshots refer to $t = 200$.

must satisfy the relation:

$$\Lambda = \frac{3/\chi_{\rm m}}{a_{\rm m}^2 \epsilon P_{\rm m}}, \tag{27}$$

where $P_{\rm m}$ is the magnetic Prandtl number and $\chi_{\rm m}$, $a_{\rm m}$ and ϵ were defined in Section 2. For anisotropy and diffusivity values around unity, we expect $\Lambda \sim 1/\epsilon$, which strengthens the choice of neglecting the viscous torque. Note that this is the appropriate Λ value to have a correct field bending ($\mathcal{R}_{\rm m} \sim 1/\epsilon$) for a unitary Prandtl number (see equation 16 in Casse & Ferreira 2000a). None the less for low diffusivity values, since $\Lambda \sim (\chi_{\rm m} a_{\rm m}^2)^{-1}$, one needs larger values of anisotropy to obtain the same torque ratio. As shown in Table 1, the values of cases 5 and 6 are chosen to satisfy such condition.

Essentially, lower magnetic diffusion increases the advection of the foot points towards the faster rotating inner part of the disc altering the dynamics of the field line. This can be seen in Fig. 13 (first panel). It is a snapshot of the field's evolution for $\alpha = 0.1$ at $t = 200$. This has already been discussed in Zanni et al. (2007). Note also that, when compared with fig. 2 of the aforementioned work, the choice of an anisotropy parameter $\chi_{\rm m} = 3$ instead of 1 allows for more diffusion of the toroidal magnetic field component. Such an effect will then result in a weaker magnetic torque F_L, lowering thus the accretion rate tending to balance the foot point's advection.

In the case of highly anisotropic configurations (i.e. second panel in Fig. 13), the topology of the magnetic field resembles that of case 2, much more similar to the analytical solutions. The diffusion of the toroidal magnetic field has two consequences: by decreasing the torque, it reduces the accretion speed and therefore the field advection; it weakens the vertical Lorentz force that would otherwise distort the field lines. As expected, the asymptotic value of the accretion rate drops from $\dot{M}_{\rm acc} = 0.13$ for case 5 (significantly larger than that of case 2) to $\dot{M}_{\rm acc} = 0.04$ for case 6.

In the second set of panels on the right-hand side of Fig. 13, the logarithmic ratio $|B_\phi|/B_{\rm p}$ is displayed in the same fashion as in Fig. 4. It is clear that for case 5 this ratio takes high values as expected by fig. 5 in Zanni et al. (2007). This is an indication of the swift dominance of the poloidal component of the Lorentz. As the anisotropy increases (case 6), the ratio settles to values approximate to those of case 2.

In both the configurations, the outflow is accelerated to poloidal speeds close to and just above the Keplerian velocity with case 5 being somewhat slower ($\sim 1.05 V_{\rm K0}$ at $r = 2r_{\rm in}$) than case 6 ($\sim 1.35 V_{\rm K0}$ at $r = 2r_{\rm in}$). Although the highly anisotropic configuration appears to settle towards a quasi-stationary state, the terminal velocity reached is less than that of case 2, whereas the ejection efficiency takes considerably larger values, namely $\dot{M}_{\rm ej}/\dot{M}_{\rm acc} \sim 0.2$. These make this setup less optimal in comparison to case 2. Therefore, it is confirmed that the requirement of an anisotropic magnetic diffusivity (small degrees for high α but quite large for low-α configurations) proposed in Ferreira & Pelletier (1995) is crucial in order to obtain a stationary solution; however, non-stationary solutions of possible astrophysical interest can be found without it.

5 CONCLUSIONS

We have presented a series of simulations to investigate the evolution of an axisymmetrically rotating accretion disc with respect to a set of initial magnetizations – parametrized in our study as $\mu = B^2/2P$ – that spans from subequipartition to magnetical dominance. In all cases, a disc-driven outflow is formed by the magnetocentrifugal mechanism proposed by Blandford & Payne (1982). The angular momentum of the accretion disc is efficiently extracted by the outflow's magnetic torque. It is then stored in the toroidal magnetic field that in turn accelerates the plasma to form a supersonic – and in large sample of cases a super-Alfvénic/superfast magnetosonic – jet. We have found the efficiency and behaviour of this mechanism to be strongly dependent on the magnetization of the disc. The same holds for many important aspects of the outflow, as well as the progress of the driving element itself: the magnetic field, that we assumed to be initially purely poloidal.

Collimation and ejection efficiency. The magnetic field lines reach a more collimated configuration for large magnetizations. This is a combined effect of an inward Lorentz force (lower panel of Fig. 6) and the decrease of the magnetic Raynolds number due to a smaller accretion velocity and the increase of magnetic resistivity. A study of the magnetic flux function that labels the field lines show both an inward motion in the upper part of the domain and an outward slip inside the resistive disc (only for above equipartition cases). The accreting matter which is responsible of the field's bending can cross the magnetic field lines more easily and shows smaller accretions rates, thus it cannot really support the initial curvature in a prolonged manner.

Moreover, after the initial transient phase, the ejection efficiency and the ejection index (analogous to the mass load) increase with μ. As shown in Ferreira (1997), such a behaviour can be attributed in a decrease of the field's curvature and a smaller pinching associated with B_ϕ. For cases of magnetization above equipartition, on the later stages of the simulations the resulting magnetic field above the disc is almost perpendicular to the meridional plane. In contrast, the subequipartition cases settle in an open field topology. The weaker field case is somewhat inefficient in the collimation of the field lines anchored on the outermost part of the ejection region.

Acceleration mechanism. The magnetocentrifugal mechanism can be broken down to two phases: an initial centrifugal acceleration from the disc up to roughly the Alfvén critical surface (which is magnetically driven mainly by the toroidal Lorentz force) and a poloidal drive (mostly due to the gradient of magnetic pressure) above it. We have established that this is the case for our solutions (Fig. 6): above the slow magnetosonic point, the force that drives the flow along a given field line is centrifugal. At higher altitudes, the poloidal component of the Lorentz force catches up (just before the Alfvén point) and remains the main driving force from then on. Thermal forces (due to poloidal pressure gradients), even though

assist in the deviation of the accreting matter on to the field line, do not play an important role in the acceleration itself.

Moreover, it has been shown (Ferreira 1997) that the directional components of the Lorentz force can be associated with the toroidal-to-poloidal magnetic field ratio (equation 14). Since the toroidal component of the Lorentz force is responsible for the centrifugal drive, whereas the poloidal component prevails in the non-corotating region, their ratio provides a useful diagnostic to estimate the impact of each phase. We have shown that for weakly magnetized configurations the poloidal drive quickly overcomes the centrifugal one, as the Alfvén surface is easily crossed at small altitudes (Figs 4 and 11). None the less, a great part of the acceleration happens in the sub-Alfvénic region, where the toroidal acceleration dominates (Figs 6 and 8). The situation changes for high-μ configurations (Fig. 4); even though the ejection efficiency increases, the magnetic field's strength does not allow the bending of the field lines. These cases present only a minor twisting (small B_ϕ), while the magnetic surfaces are almost cylindrical. This results in a situation where $F_{L;\phi} > F_{L;P}$ but the centrifugal acceleration is *not* efficient, since the inclination of the field lines is too small.

Terminal velocities and critical surfaces. The magnetic acceleration gives higher terminal velocities for values of the magnetization parameter just below equipartition (Fig. 8). Even lower values of μ can give satisfactory results, but the outflow is somewhat slower. For strongly magnetized discs, the resulting outflow expands initially faster than for low-magnetization cases (Fig. 3), but the velocity is not sustained (Fig. 5). Essentially, the strong coupling with the corona and the prominent magnetic braking extracts a large part of the angular momentum available in the initial expansion. This leads to a slower rotation of the underlying disc that results inadequate to accelerate the jet permanently. The outflow can cross the critical surfaces (Alfvén and fast magnetosonic) only if the magnetization is below equipartition (Figs 5 and 11).

Current-carrying outflows regarding the current carried by the outflow, stationary analytical studies predict a butterfly-like circuit. This has been confirmed only for low-magnetization configurations (Figs 3 and 11). In highly magnetized cases, the outflowing current has no clear order. The counterclockwise direction of the poloidal current and the decomposition of the Lorentz force perpendicular and parallel to the circuit fit well with the evolution of the magnetic field. In fact, we observe collimation in the inner part of the ouflow (caused by the hoop stress) and decollimation in the outer part (caused by the poloidal gradient of magnetic pressure). It goes without saying that this is true only for cases 1 and 2.

Quasi steady state. The clear plateau in the ejection efficiency (Fig. 7) and the invariance of the MHD integrals (Fig. 10) advocates in favour of the quasi-stationarity of the solutions for magnetization below equipartition. It is also clear that no such claim can be made for the strongly magnetized cases. This statement applies only to the innermost part of the magnetized disc, since the revolutions of the outer part are not enough to reach a quasi-stationary state. This has already been discussed in Zanni et al. (2007).

Disc behaviour and accretion. The accretion disc retains more or less its geometrical thickness for subequpartition magnetic fields. For strong magnetization, the pinching from the Lorentz force (due to the toroidal field) in the initial phases of the simulations and the elevated values of ejection rates result in a thinner disc. The disc's slowdown is more prominent as the magnetic braking and the coupling with the corona is stronger. This leads to a swift extraction of angular momentum and mass (as the ejection efficiency increases with the magnetization), answering in part for the disc becoming more flat. None the less, the sustained extraction of angular momentum for low-magnetization cases results in higher accretion rates.

High anisotropy. As discussed in Zanni et al. (2007), the choice of magnetic resistivity has a major impact in the accretion–ejection mechanism, leading, for small diffusivity values, to a distorted magnetic field topology. This is caused by the twisting of the field lines advected towards the faster rotating inner radii of the disc. Incited by the analytical predictions of Casse & Ferreira (2000a), we have shown that such low-α configurations require very high anisotropy in order to diffuse the toroidal field component and obtain an ordered B-field topology (Fig. 13). None the less, such extremely anisotropic resistivity configurations are less adequate to describe the observed outflows. The terminal velocity reached is smaller and the ejection efficiency much larger than that expected from such sources.

ACKNOWLEDGMENTS

We would like to thank the anonymous reviewer for many insightful suggestions and remarks that significantly improved this article. PT would also like to thank N. Vlahakis, K. Tsinganos and T. Matsakos for many fruitful discussions and comments. AF thanks R. Rosner and D. Lamb for hospitality and support at the University of Chicago. This work was supported in part by the U.S. DoE under grant No. B523820 to the Center of Astrophysical Thermonuclear Flashes at the University of Chicago and the EU Marie Curie Research Training Network JETSET under contract MRTN-CT-2004-005592. Part of the simulations has been performed at the clusters provided by CINECA, Bologna, Italy.

REFERENCES

Blandford R. D., 1976, MNRAS, 176, 465
Blandford R. D., Payne D. G., 1982, MNRAS, 199, 883
Bessolaz N., Zanni C., Ferreira J., Keppens R., Bouvier J., 2008, A&A, 478, 155
Casse F., Ferreira J., 2000a, A&A, 353, 1115
Casse F., Ferreira J., 2000b, A&A, 361, 1178
Casse F., Keppens R., 2002, ApJ, 581, 988
Casse F., Keppens R., 2004, ApJ, 601, 90
Contopoulos J., Lovelace R. V. E., 1994, ApJ, 429, 139
Ferreira J., Pelletier G., 1995, A&A, 295, 807
Ferreira J., 1997, A&A, 319, 340
Kato S. X., Kudoh T., Shibata K., 2002, ApJ, 565, 1035
Königl A., 2004, ApJ, 617, 1267
Krasnopolsky R., Li Z. Y., Blandford R. D., 1999, ApJ, 526, 631
Li Z-Y., 1995, ApJ, 444, 848
Londrillo P., Del Zanna L., 2004, J. Comput. Phys, 195, 17
Lovelace R. V. E., 1976, Nat, 262, 649
Lovelace R. V. E., Berk H. L., Contopoulos J., 1991, ApJ, 379, 696
Matsakos T., Tsinganos K.Vlahakis N., Massaglia S., Mignone A., Trussoni E., 2008, A&A, 477, 521
Meliani Z., Casse F., Sauty C., 2006, A&A, 460, 1
Mignone A., Bodo G., Massaglia S., Matsakos T., Tesileanu O., Zanni C., Ferrari A., 2007, ApJS, 170, 228
Ogilvie G. I., Livio M., 2001, ApJ, 553, 158
Ouyed R., Pudritz R. E., 1997, ApJ, 482, 712
Romanova M. M., Ustyugova G. V., Koldoba A. V., Lovelace R. V. E., 2005, ApJ, 635, L165
Romanova M. M., Kulkarni A. K., Lovelace R. V. E., 2008, ApJ, 673, 171
Romanova M. M., Ustyugova G. V., Koldoba A. V., Lovelace R. V. E., 2009, MNRAS, in press (arXiv:0901.4265v1)
Shakura N. I., Sunyaev R. A., 1973, A&A, 24, 337
Tsinganos K., 1982, ApJ, 252, 775
Uchida Y., Shibata K., 1985, PASJ, 37, 515

Ustyugova G. V., Koldoba A. V., Romanova M. M., Chechetkin V. M., Lovelace R. V. E., 1995, ApJ, 439, L39
Ustyugova G. V., Koldoba A. V., Romanova M. M., Chechetkin V. M., Lovelace R. V. E., 1999, ApJ, 516, 221
Ustyugova G. V., Koldoba A. V., Romanova M. M., Lovelace R. V. E., 2006, ApJ, 646, 304
Vlahakis N., Tsinganos K., 1998, MNRAS, 298, 777
Wardle M., Königl A., 1993, ApJ, 410, 218
Zanni C., Ferrari A., Massaglia S., Bodo G., Rossi P., 2004, Ap&SS, 293, 99
Zanni C., Ferrari A., Rosner R., Bodo G., Massaglia S., 2007, A&A, 469, 811

APPENDIX A: UNITS AND NORMALIZATION

Each primitive variable, namely ρ, P, $\boldsymbol{u}$, $\boldsymbol{B}$, are normalized for computational convenience, with respect to fiducial values. The choice of these values is arbitrary, but we select scales that can efficiently describe the problem. Thus, all lengths are normalized to the truncation radius of the disc, $r = r_0$ and speeds to the Keplerian velocity calculated at r_0. This choice dictates a time unit equal to $t_0 = r_0/V_{\rm K0}$. Density is normalized with respect to the initial density ρ_0 at the disc's mid-plane and at the truncation radius. From the equation of state, the resulting P_0 will be equal to ϵ^2 whereas from the momentum equation we get $B_0 = B_{z0} = \epsilon\sqrt{2\mu}$. The corresponding units in YSO and AGN disc jet systems are stated below:

$$r_0 = 0.1\ \text{au} \qquad \text{(YSO)}$$
$$= 10R_{\rm Schw} = 10^{-4}\left(\frac{M}{10^8\,{\rm M}_\odot}\right)\ \text{pc} \quad \text{(AGN)}, \tag{A1}$$

where $R_{\rm Schw} = 2GM/c^2$ is the Swarzschild radius of the AGN. The Keplerian velocity will be

$$V_{\rm K0} = 94\left(\frac{M}{{\rm M}_\odot}\right)^{\frac{1}{2}}\left(\frac{r_0}{0.1\,\text{au}}\right)^{-\frac{1}{2}}\ \text{km s}^{-1} \qquad \text{(YSO)}$$
$$= 6.7\times10^4\left(\frac{r_0}{10R_{\rm Schw}}\right)^{-\frac{1}{2}}\ \text{km s}^{-1} \qquad \text{(AGN)}. \tag{A2}$$

Given these scalings, the period of rotation at the inner disc radius will be 2and since $t_0 = r_0/V_{\rm K0}$ the time unit will be

$$t_0 = 1.7\left(\frac{M}{{\rm M}_\odot}\right)^{-\frac{1}{2}}\left(\frac{r_0}{0.1\,\text{au}}\right)^{\frac{3}{2}}\ \text{d} \qquad \text{(YSO)}$$
$$= 0.5\left(\frac{M}{10^8\,{\rm M}_\odot}\right)\left(\frac{r_0}{10R_{\rm Schw}}\right)^{\frac{3}{2}}\ \text{d} \qquad \text{(AGN)}. \tag{A3}$$

Density is normalized through the choice of a suitable mass accretion rate $\dot{M}_0 = r_0^2\rho_0 V_{\rm K0}$

$$\dot{M}_0 = 3\times10^{-7}\left(\frac{\rho_0}{10^{-12}\,\text{g cm}^{-3}}\right)\left(\frac{M}{{\rm M}_\odot}\right)^{\frac{1}{2}}\left(\frac{r_0}{0.1\,\text{au}}\right)^{\frac{3}{2}}\ {\rm M}_\odot\ \text{yr}^{-1}$$
$$= 9\left(\frac{\rho_0}{10^{-12}\,\text{g cm}^{-3}}\right)\left(\frac{M}{10^8\,{\rm M}_\odot}\right)^{2}\left(\frac{r_0}{10R_{\rm Schw}}\right)^{\frac{3}{2}}\ {\rm M}_\odot\ \text{yr}^{-1}. \tag{A4}$$

Torques and forces will be given in units $\dot{J}_0 = r_0^3\rho_0 V_{\rm K0}^2$ and $\dot{E}_0 = r_0^2\rho_0 V_{\rm K0}^3$ in (dyne cm) and (erg s^{-1}), respectively.

$$\dot{J}_0 = 3\times10^{38}\left(\frac{\rho_0}{10^{-12}\,\text{g cm}^{-3}}\right)\left(\frac{M}{{\rm M}_\odot}\right)\left(\frac{r_0}{0.1\,\text{au}}\right)^{2}$$
$$= 1.2\times10^{51}\left(\frac{\rho_0}{10^{-12}\,\text{g cm}^{-3}}\right)\left(\frac{M}{10^8\,{\rm M}_\odot}\right)^{3}\left(\frac{r_0}{10R_{\rm Schw}}\right)^{2} \tag{A5}$$

$$\dot{E}_0 = 1.9\times10^{33}\left(\frac{\rho_0}{10^{-12}\,\text{g cm}^{-3}}\right)\left(\frac{M}{{\rm M}_\odot}\right)^{\frac{3}{2}}\left(\frac{r_0}{0.1\,\text{au}}\right)^{\frac{1}{2}}$$
$$= 2.6\times10^{46}\left(\frac{\rho_0}{10^{-12}\,\text{g cm}^{-3}}\right)\left(\frac{M}{10^8\,{\rm M}_\odot}\right)^{2}\left(\frac{r_0}{10R_{\rm Schw}}\right)^{\frac{1}{2}}. \tag{A6}$$

The choice of the ϵ parameter defines the initial thermal height scale of the disc and the scaling of temperature in the mid-plane will be given by $T_{z=0} = \epsilon^2\frac{m_{\rm p}GM}{Kr}$

$$T_{z=0} = 10^4\left(\frac{\epsilon}{\epsilon_0}\right)^2\left(\frac{M}{{\rm M}_\odot}\right)\left(\frac{r}{0.1\,\text{au}}\right)^{-1}\text{K} \qquad \text{(YSO)}$$
$$= 5\times10^9\left(\frac{\epsilon}{\epsilon_0}\right)^2\left(\frac{r}{10R_{\rm Schw}}\right)^{-1}\text{K} \qquad \text{(AGN)} \tag{A7}$$

On the other hand, the choice of the magnetization parameter will determine the strength of the poloidal magnetic field at the equator $B_{z=0} = \sqrt{\mu\,8\pi\,P}$ that reads in Gauss

$$B_0 = 2.6\left(\frac{\mu}{\mu_0}\right)^{\frac{1}{2}}\left(\frac{\epsilon}{\epsilon_0}\right)\left(\frac{M}{{\rm M}_\odot}\right)^{\frac{1}{2}}\left(\frac{\rho_0}{10^{-12}\,\text{g cm}^{-3}}\right)^{\frac{1}{2}}\left(\frac{r}{0.1\,\text{au}}\right)^{-\frac{5}{4}}$$
$$= 1.8\times10^3\left(\frac{\mu}{\mu_0}\right)^{\frac{1}{2}}\left(\frac{\epsilon}{\epsilon_0}\right)\left(\frac{\rho_0}{10^{-12}\,\text{g cm}^{-3}}\right)^{\frac{1}{2}}\left(\frac{r}{10R_{\rm Schw}}\right)^{-\frac{5}{4}}. \tag{A8}$$

This paper has been typeset from a TEX/LATEX file prepared by the author.